Geomechanics and Engineering, *Vol. 20, No. 5 (2020) 399-410*
DOI: https://doi.org/10.12989/gae.2020.20.5.399

Experimental study on the mechanical response and failure behavior of double-arch tunnels with cavities behind the liner

Xu Zhang[1,2], Chengping Zhang*[2,3], Bo Min[2,3] and Youjun Xu[1,2]

[1]*School of Civil Engineering, Inner Mongolia University of Science and Technology, Baotou 014000, China*
[2]*Key Laboratory of Urban Underground Engineering of Ministry of Education, Beijing Jiaotong University, Beijing 100044, China*
[3]*School of Civil Engineering, Beijing Jiaotong University, Beijing 100044, China*

(Received October 27, 2019, Revised January 30, 2020, Accepted February 6, 2020)

Abstract. Cavities often develop behind the vault during the construction of double-arch tunnels, generally in the form of various defects. The study evaluates the impact of cavities behind the vault on the mechanical and failure behaviors of double-arch tunnels. Cavities of the same sizes are introduced at the vault and the shoulder close to the central wall of double-arch tunnels. Physical model tests are performed to investigate the liner stress variation, the earth pressure distribution and the process of progressive failure. Results reveal that the presence of cavities behind the liner causes the re-distribution of the earth pressure and induces stress concentration near the boundaries of cavities, which results in the bending moments in the liner inside the cavity to reverse sign from compression to tension. The liner near the invert becomes the weak region and stress concentration points are created in the outer fiber of the liner at the bottom of the sidewall and central wall. It is suggested that grouting into the foundation soils and backfilling injection should be carried out to ensure the tunnel safety. Changes in the location of cavities significantly impact the failure pattern of the liner close to the vault, e.g., cracks appear in the outer fiber of the liner inside the cavity when a cavity is located at the shoulder close to the central wall, which is different from the case that the cavity locates at the vault, whereas changes in the location of cavities have a little influence on the liner at the bottom of the double-arch tunnels.

Keywords: double-arch tunnel; cavity; liner stress; earth pressure; crack; safety factor; physical model test

1. Introduction

For the past few years, the safety of tunnel construction, especially the tunnel face stability analysis, has been a hot topic in the tunnel engineering (Do *et al.* 2014, Fahimifar *et al.* 2015, Yang and Yan 2015, Zhang *et al.* 2015, Li *et al.* 2019, Mansouri and Asghari-Kaljahi 2019, Li and Zhang 2020, Zhang *et al.* 2020). However, several defects during the service life of tunnels have aroused widespread attention. Erosion voids generally develop near the springline or the invert of concrete pipes (Meguid and Kamel 2014), whereas based on the detecting results (Lai *et al.* 2017, Yasuda *et al.* 2017, Ye *et al.* 2020), cavities often develop behind the liner especially near the vault during the tunnel construction. One of the important goals of detecting highway or railway tunnels is to reveal cavities. Different test methods, such as ground-penetrating radar scanning (Kravitz *et al.* 2019), the impulse response method (Voznesenskii and Nabatov 2017), and in situ microtremor measurements (Gao *et al.* 2014), play an important part in detecting cavities, which form for various reasons: improper backfilling, transport vibrations, water erosion, and natural karsts (Jones and Hunt 2011, Meguid and Kamel 2014). The presence of cavities can induce the concentration of stress near the boundaries of cavities, and cause deterioration of the liner as well as the formation of liner cracks, water leakage, and steel-bar corrosion (Wang *et al.* 2014, Shi and Li 2015, Kang *et al.* 2017).

For a tunnel, Leung and Meguid (2011) conducted that changes in earth pressure differed greatly depending upon the location of cavities. Xin *et al.* (2018) performed shaking table tests on tunnels with and without cavities on the crown and found that unexpected high tension strains and annular cracks occurred. Ding *et al.* (2019) revealed that the liner with a large cavity corresponded to low bearing capacity and great deformation near the cavity. However, model tests have several shortcomings, e.g., time-consuming, high cost, and poor flexibility. Some studies have evaluated the effect of cavities numerically. Meguid and Dang (2009) evaluated the influence of cavities on the liner circumferential stresses and revealed that bending moments could reverse signs for large-size cavities. Xu *et al.* (2019b) investigated the failure process of the liner with cavities at different locations based on the discrete-continuous coupling method. Zhao *et al.* (2019) studied the stress distribution and failure behavior of the liner in the railway tunnel induced by cavities. Previous numerical studies focus on the possible locations of cracks from the perspective of stress by qualitative analysis, which is a lack of knowledge of the destructive evolution process of the liner. Yasuda *et al.* (2017) presented two-dimensional (2D) elastic solutions for a deep circular tunnel with a cavity under far-field static loading. Soon after, Yasuda *et al.* (2019) presented the three-dimensional (3D) elastic solutions for a deep cylindrical tunnel under the influence of a cavity subjected to seismic waves.

*Corresponding author, Ph.D., Professor
E-mail: chpzhang@bjtu.edu.cn

ISSN: 2005-307X (Print), 2092-6219 (Online)

For double-arch tunnels, Lai *et al.* (2017) revealed that insufficient thickness, cavities, cracks, and water leakage were encountered during the service life of the Shitigou Tunnel. Other researchers have been devoted to examining the performance of the liner of double-arch tunnels during construction in terms of field investigation (Zhang *et al.* 2017, Yan *et al.* 2017), numerical simulation (Li *et al.* 2008, Huang *et al.* 2010), and laboratory model tests (Wang *et al.* 2016, Li *et al.* 2016). Min *et al.* (2018) concluded the 2D numerical simulation using the extended finite element method (XFEM) to analyze the liner failure of the double-arch tunnels with a cavity located at the central wall. Zhang *et al.* (2019) conducted numerical analyses to investigate the lining internal force and the lining failure induced by the cavities introduced at different locations of the symmetrical double-arch tunnels. Tunnel design leaves the presence of cavities behind the liner especially close to the vault out of consideration due to cavities generally associated with poor construction. Thus, it is essential to find out the influence of cavities on the safety of the double-arch tunnels.

In the current paper, two physical model tests of double-arch tunnels with cavities at different locations were carried out. Experimental results provide insight into the liner stress variation, the earth pressure re-distribution, and the failure pattern of the tunnel liner with regard to different locations of cavities. And then, the effects of the cavities on the safety of the double-arch tunnels were revealed. Finally, several preventive measures, which were primarily designed to reinforce the ground and fill cavities, are introduced.

2. Physical model tests

2.1 The similarity theorem and similarity material

According to the similarity laws and the results of the physical modeling of tunnels (Meguid *et al.* 2008), the ratio of similitude (C) is deduced with theoretical analysis (Lei *et al.* 2015). These equilibrium differential equations of the prototype tunnel (marked with subscript "s") and the model tunnel (marked with subscript "m") are expressed as:

$$\begin{cases} \dfrac{\partial(\sigma_x)_i}{\partial_{xi}}+\dfrac{\partial(\tau_{xy})_i}{\partial_{yi}}+\dfrac{\partial(\tau_{xz})_i}{\partial_{zi}}=0 \\ \dfrac{\partial(\tau_{yz})_i}{\partial_{xi}}+\dfrac{\partial(\sigma_y)_i}{\partial_{yi}}+\dfrac{\partial(\tau_{yz})_i}{\partial_{zi}}=0 \quad ,i=\mathrm{s,m} \\ \dfrac{\partial(\tau_{xz})_i}{\partial_{xi}}+\dfrac{\partial(\tau_{yz})_i}{\partial_{yi}}+\dfrac{\partial(\sigma_z)_i}{\partial_{zi}}-\gamma_i=0 \end{cases} \tag{1}$$

Poisson's ratio μ is the ratio of transverse contraction strain to longitudinal extension strain in the direction of the stretching force. The shear strength (τ_f) of a soil at a point on a particular plane was expressed by Coulomb as a linear function of the normal stress at failure (σ_f) on the plane at the same point: $\tau_f = c + \sigma_f \tan\varphi$ (Chenari *et al.* 2019), where cohesion c and internal friction angle φ for the soil is the shear strength parameters referred to as the cohesion intercept and the angle of shearing resistance, respectively.

Symbolizing the similarity ratio of geometry size L, stress σ, strain ε, displacement δ, gravity γ, elastic modulus E, Poisson's ratio μ, cohesion c, and internal friction angle φ with C_L, C_σ, C_ε, C_δ, C_γ, C_E, C_μ, C_c, and C_φ respectively.

$$\begin{cases} C_\sigma=\dfrac{(\sigma_x)_\mathrm{s}}{(\sigma_x)_\mathrm{m}}=\dfrac{(\sigma_y)_\mathrm{s}}{(\sigma_y)_\mathrm{m}}=\dfrac{(\sigma_z)_\mathrm{s}}{(\sigma_z)_\mathrm{m}} \\ C_\sigma=\dfrac{(\tau_{xy})_\mathrm{s}}{(\tau_{xy})_\mathrm{m}}=\dfrac{(\tau_{yz})_\mathrm{s}}{(\tau_{yz})_\mathrm{m}}=\dfrac{(\tau_{zx})_\mathrm{s}}{(\tau_{zx})_\mathrm{m}} \\ C_L=\dfrac{x_\mathrm{s}}{x_\mathrm{m}}=\dfrac{y_\mathrm{s}}{y_\mathrm{m}}=\dfrac{u_\mathrm{s}}{u_\mathrm{m}}=\dfrac{l_\mathrm{s}}{l_\mathrm{m}} \\ C_E=\dfrac{E_\mathrm{s}}{E_\mathrm{m}},C_\mu=\dfrac{\mu_\mathrm{s}}{\mu_\mathrm{m}},C_\gamma=\dfrac{\gamma_\mathrm{s}}{\gamma_\mathrm{m}} \end{cases} \tag{2}$$

Substituting the similarity ratios into the basic equation of elastic mechanics (Huang *et al.* 2013, Lei *et al.* 2015, Fang *et al.* 2018), the relationship is as below:

$$C_\sigma = C_L \cdot C_\gamma, C_E = C_L \cdot C_\gamma \tag{3}$$

Thereby attaining the similarity criterion for model tests:

$$C_\sigma/(C_L \cdot C_\gamma)=1, C_E/(C_L \cdot C_\gamma)=1 \tag{4}$$

Depending on the model dimensions and experimental conditions, the selected geometry size and gravity similarity ratios are 40:1 and 1:1, respectively, that is, $C_L = 40$ and $C_\gamma = 1$. Consequently, the other similarity parameters can be determined as follows: $C_\mu = C_\varphi = C_\varepsilon = 1$ and $C_\delta = C_E = C_c = C_\sigma = 40$, where C_μ, C_φ, C_ε, C_δ, C_E, C_c, and C_σ represent the similarity ratio of μ, φ, ε, δ, E, c and σ.

In the light of failure tests in the model, the loads were applied gradually until the structures failed, i.e., loss of the carrying capacity, but not limited to the elastic ranges. The requirements of similarity should be met: Firstly, strain in the prototype is the same as that in the model, i.e., each part maintains geometric similarity all the time. Secondly, the strength of materials both of them satisfies the complete similarity, i.e., similar Mohr failure envelope. Finally, the stress-strain relationship of materials is similar. Due to the limitation of the testing technology and devices, the above-mentioned conditions are difficult to realize simultaneously. Based on a highway double-arch tunnel, the prototype referred is surrounding rock of grade V in the soft ground according to the road tunnel design specification (Ministry of Communications of the People's Republic of China, 2004). In consideration of the scale effect of failure tests in the model, the similarity materials have the characteristics of high unit weight and low strength and elastic modulus, which could meet the requirements of the full similarity and the scaling model size (Fang *et al.* 2018, Zhang *et al.* 2019).

Based on the previous work on analogous soils (Meguid *et al.* 2008, Li *et al.* 2017, Huang *et al.* 2018), a type of acceptable material of the soils of the model is developed for satisfying the similarity requirements, that is, the soils of the model were made from a mixture of barite powder, silica sand and petroleum jelly in a weight ratio of 4:10:1. The similar material of soils uses the barite powder or blanc fixe with a chemical composition of $BaSO_4$ and silica sand with a chemical composition of SiO_2 as its aggregate, and

Table 1 Mechanical parameters of prototype and model materials

		Unit weight (kN / m^3)	Elastic modulus (GPa)	Poisson's ratio	Cohesion (kPa)	Friction angle (°)
Soil	Prototype	18	0.27	0.37	182	24
	Model	18	0.0068	0.37	4.6	24
Liner	Prototype	25	33.5	0.20	—	—
	Model	8.3	0.8350	0.20	—	—

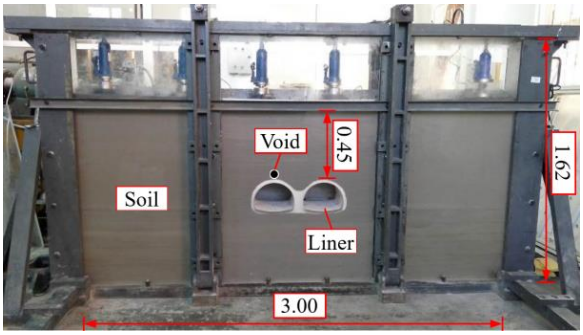

Fig. 1 Model test apparatus (unit: m)

petroleum jelly or Vaseline as its cementing agents.

Jin *et al.* (2019) revealed that the existence of the scale effect had been confirmed by a series of experiments until the brittle failure of the geometrically-similar concrete materials and reinforced concrete members occurred. The mechanical property of concrete is generally consistent with gypsum based on fracture mechanics. For failure tests, the gypsum as a hard brittle material is generally adopted to simulate the underground and hydraulic structures. It is worth noting that the materials of structures in the model are composed of the homogeneous elastic materials, which can not completely reflect the reliability of actual materials.

The liner in the prototype is mainly made up of the C40 concrete. Through uniaxial compressive strength tests on cylinders with different ratios, a mixture of water and gypsum in a weight ratio of 0.9:1, which is the one closest to the similarity criterion were selected. The features of fracture mechanics of the mixture of water and gypsum as the model materials, which are regarded as liner materials (Lei *et al.* 2015, Wang *et al.* 2019, Su *et al.* 2020), are basically similar to those of the concrete. Note that the unit weight of the liner in the model is not completely consistent with the prototype. However, the influence of the unit weight was negligible (Min *et al.* 2018). The parameters of prototype and model materials are shown in Table 1.

2.2 Experimental apparatus

Physical model tests were performed in a tank, which was composed of a series of removable steel frame sections, with dimensions of 3.00 m in width and 1.62 m in height in the transverse direction during the tunnel excavation. The thickness of the tank (the distance between the front and back wall) in the direction of the tunnel excavation is 0.3 m. Because the test apparatus with the sufficient stiffness has the loading bearing capacity of more than 0.30 MPa and the deformation is less than 3 mm, the rigid constraint was basically applied in the tunneling direction. The bottom surface is fixed on a steel plate and the front sidewall is conducted using the transparent Plexiglas plates with a thickness of 50 mm for observing the failure process during testing. Six jacks were placed on the top of the rock mass in the tank to compensate for the lack of burial depth. The external frames of the apparatus are as shown in Fig. 1. It is worth noting that the model is represented by a whole part and the middle vertical steel frames on the outside of the perspex sheets are used to restrict the top steel plate.

2.3 Experimental schemes and process

The double-arch tunnel in the prototype with a span (D) of 25.92 m and a height (H) of 9.99 m contains two single tunnels, which are regarded as the "left tunnel" and "right tunnel", as shown in Fig. 2(a). The thickness of the double-arch tunnel liner is 0.90 m. As shown in Fig. 2(b), the cross-sectional dimensions of the model are determined by the section of the prototype liner and the similarity rate. In order to place the model liner in the tank, the length of the models in the direction of the excavation is 0.295 m.

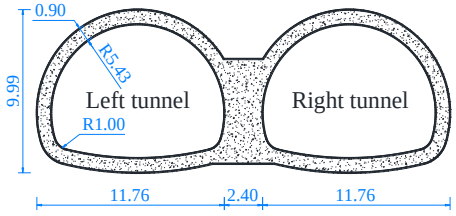

(a) Actual dimension

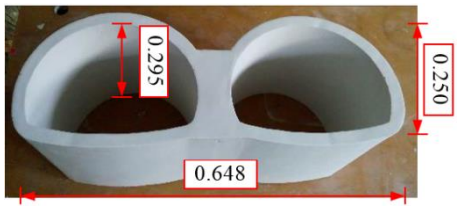

(b) Model entity

Fig. 2 Model of double-arch tunnel liner (unit: m)

(a) Model Test 1 (MT1)

(b) Model Test 2 (MT2)

Fig. 3 Scheme of model tests

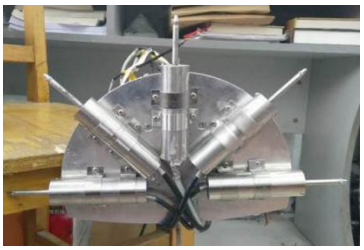

Fig. 4 Displacement testing device

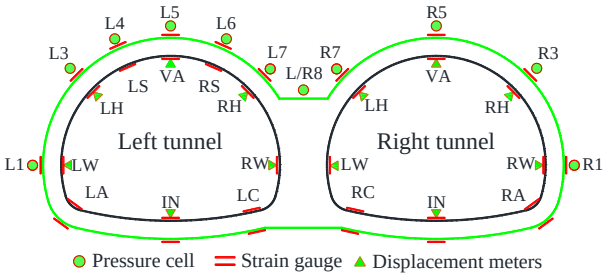

Fig. 5 Layout of MPs

Taking only the self-weight stress into account, two model tests were performed to investigate the failure pattern of double-arch tunnels with cavities at different positions, i.e., with a cavity located at the vault (Model Test 1(MT1)), and with a cavity located at the right shoulder of the left tunnel (Model Test 2 (MT2)), as shown in Fig. 3. Assuming that all the cavities have a simplified cylindrical geometry with a diameter of about 0.06 m, the tunnel span D is about eleven times the diameter of the cavity.

A series of numerical analyses were conducted to verify the experimental results without cavities and with a cavity on the top of the central wall of symmetrical double-arch tunnels and provide a reasonable basis for monitoring in this study. Monitoring components include thirty-two strain gauges fixed at the extrados and intrados of the model liner, ten pressure cells for each model test, twelve displacement meters, a crack width detector, and two depth gauges. These strain gauges were adopted to measure the circumferential strain of the liner of the double-arch tunnels in the cross-sectional direction. Six displacement meters installed in a metal plate were adopted to monitor the radial displacement of the liner, as shown in Fig. 4. Then, the twin test devices were installed inside the left and right tunnel.

The layout of measuring points (MPs) is shown in Fig. 5. The two capital letters in brackets are the abbreviation of the position of the liner. To be specific, the first letter “L” or “R” of the MP label indicates the “left” or “right”, respectively, and the second letter “H”, “S”, “W”, “A” or “C” indicates the “haunch”, “shoulder”, “sidewall”, “arch spring” or “corner of wall, respectively. In order to distinguish from the previous MP label, “VA” and “IN” indicate the “vault” and “invert” respectively. Moreover, the letter “CH” of displacement meters indicates the “Channel”.

Model tests are mainly divided into four steps: The first step is preparation. The materials were prepared, and plastic films were attached to the inner sidewalls (Fig. 6(a)). The second step is filling materials (Fig. 6(b)), while the double-arch tunnel model was embedded at the preset place. The

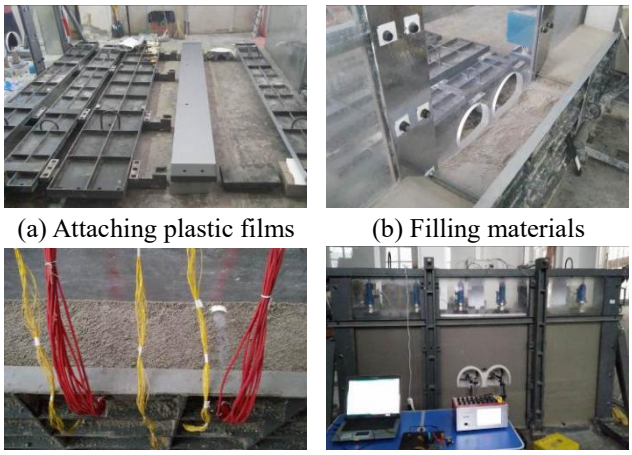

(a) Attaching plastic films (b) Filling materials

(c) Inflated bag in the ground (d) Prepared ground

Fig. 6 Process of model tests

third step is cavity formation. A cylindrical inflated bag was designed specifically for the simulation of cavity formation. The model ground was put aside for 2 days in order to make the stress and deformation of the surrounding soils trend to stabilize (Meguid *et al.* 2008, Seki *et al.* 2008, Lei *et al.* 2015). And then, the deflated inflated bag was removed from the steel plate on the back of the tank (Fig. 6(c)). Since the size of the inflated bag was small, the deformation of the ground could be ignored after the cavity was removed. The fourth step is step-by-step loading. When the prepared ground was completed, the load was gradually increased by 0.01 MPa intervals until the liner failed (Fig. 6(d)).

3. Experimental results

3.1 Liner stress variation

Change laws of the stress in the inner and outer fiber of the liner with overloads between Model Test 1 and 2 are presented in Figs. 7-8, respectively. The obatined results were magnified forty times of the measured value.

The outer stress in the liner on the corner of the central wall firstly reached the ultimate tensile strength of materials at a loading level of 0.8 MPa (0.02 MPa in the model), and the largest compressive stress occurred in the inner fiber of the liner on the corner of the central wall. In MT1, there was the larger tensile stress in the inner fiber of the liner on the right side of the cavity than that on the left side of the cavity (Figs. 7(a)-7(c)); with further increase in overloads, the stresses in the outer fiber of the liner at the vault of the left tunnel switched from tensile to compressive. The tensile stress occurred in the outer fiber of the liner on the inside of the cavity due to the concentrated load acting on both sides of the cavity. In MT2, the tensile stress in the inner fiber of the liner and the compressive stress in the outer fiber of the liner on the left side of the cavity was larger than that on the right side of the cavity (Figs. 8(a)-8(c)); with further increase in overload the stresses in the outer fiber of the liner on the inside of the cavity switched from compressive (positive) to tensile (negative), and then a crack appeared in the outer fiber of the liner on the inside of the cavity.

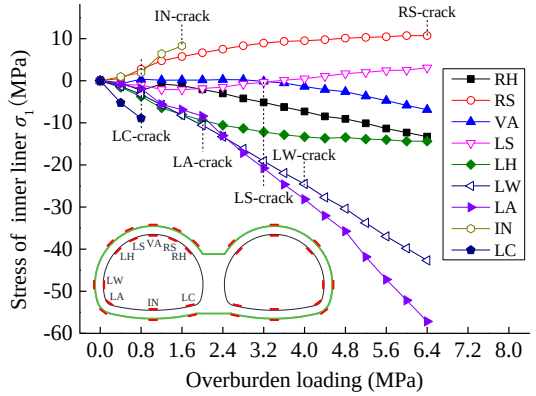

(a) Stress of the inner fiber of the liner of the left tunnel

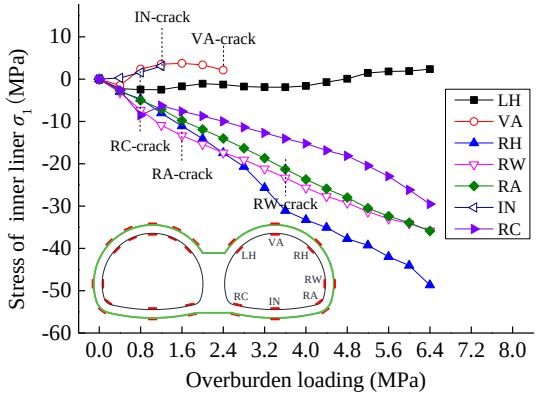

(b) Stress of the inner fiber of the liner of the right tunnel

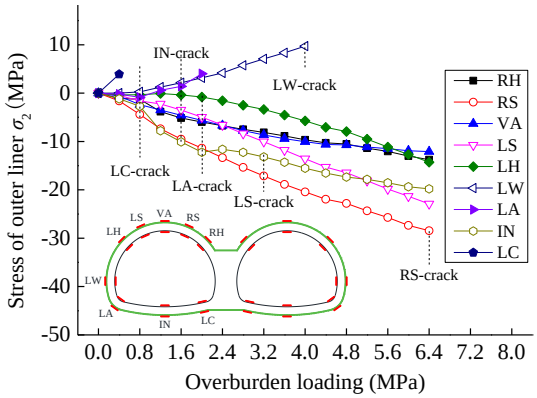

(c) Stress of the outer fiber of the liner of the left tunnel

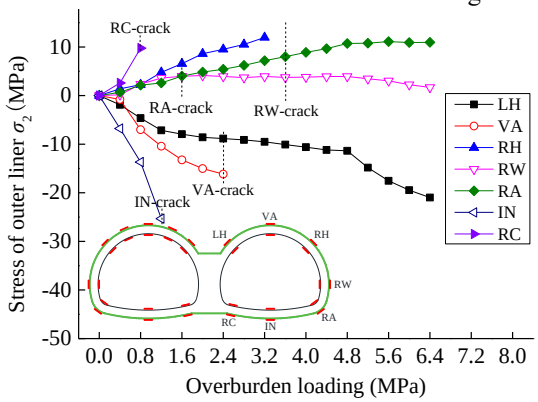

(d) Stress of the outer fiber of the liner of the right tunnel

Fig. 7 The stress of the liner with respect to the overload in MT1

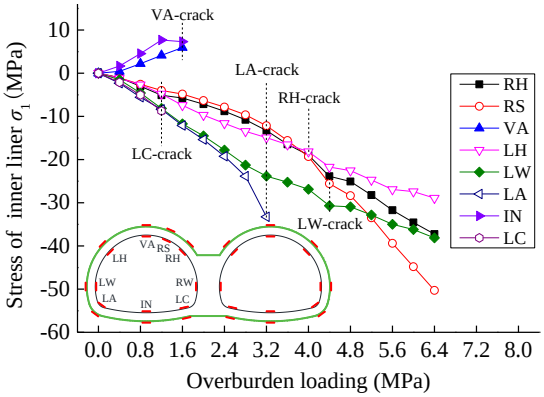

(a) Stress of the inner fiber of the liner of the left tunnel

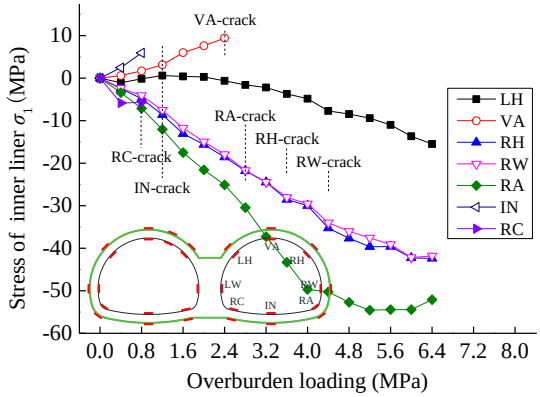

(b) Stress of the inner fiber of the liner of the right tunnel

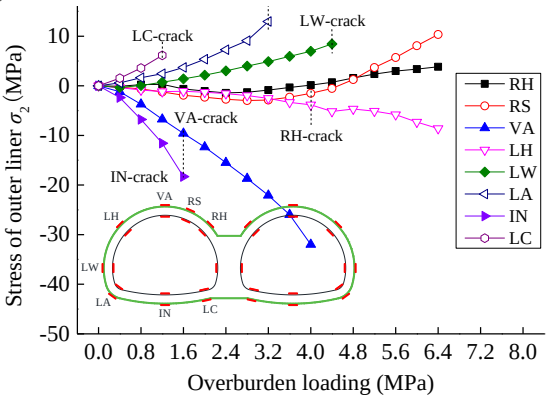

(c) Stress of the outer fiber of the liner of the left tunnel

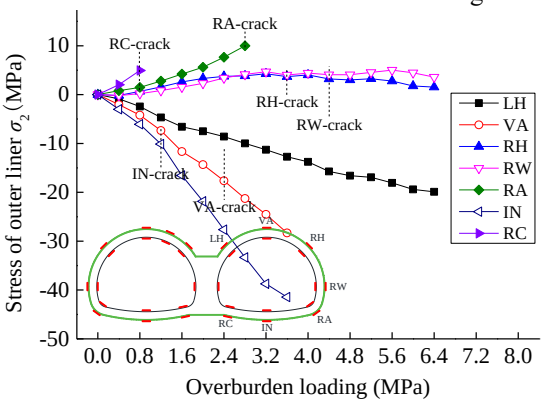

(d) Stress of the outer fiber of the liner of the right tunnel

Fig. 8 The stress of the liner with respect to the overload in MT 2

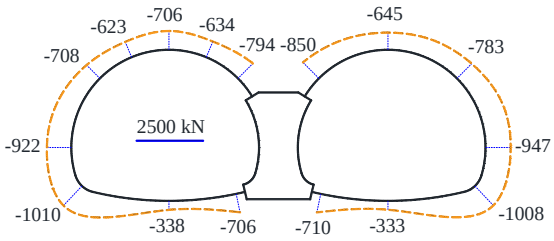

(a) MT1

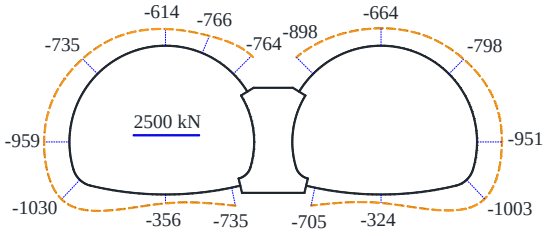

(b) MT2

Fig. 9 Thrust forces in the liner (unit: kN)

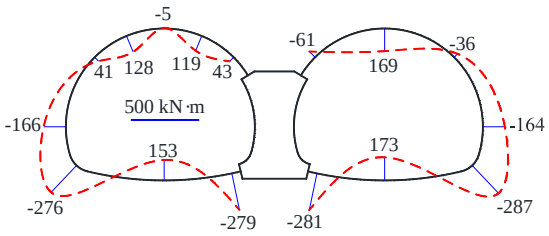

(a) MT1

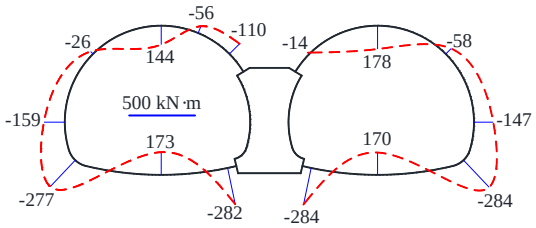

(b) MT2

Fig. 10 Bending moments in the liner (unit: kN·m)

The distribution of thrust forces and bending moments in the liner of the double-arch tunnels under the same load of 0.4 MPa is presented in Figs. 9-10, respectively. When cavities were introduced behind the liner close to the vault, the largest changes of the internal forces in the tunnel liner occurred in the liner near the cavity. Due to a lack of the reaction force of soils inside the cavity, the concentration points of the stress occurred on both sides of the cavity, which caused a significant decrease in carrying capacity of the liner on both sides of the cavity and the moments in the ring direction at the liner inside the cavity to reverse sign from compression to tension (Meguid and Kamel 2014). As shown in Fig 9, the thrust force in the liner on both sides of the cavity is -623 kN and -634 kN, respectively. Whereas the thrust force within the cavity is -706 kN in MT1. The positive and negative value indicates the "bending inwards" and "bending towards", respectively. The moments bending towards were obtained at the bottom of the central wall and the maximum value was 284 kN·m, which was larger than those at other locations. The bending moment at the liner

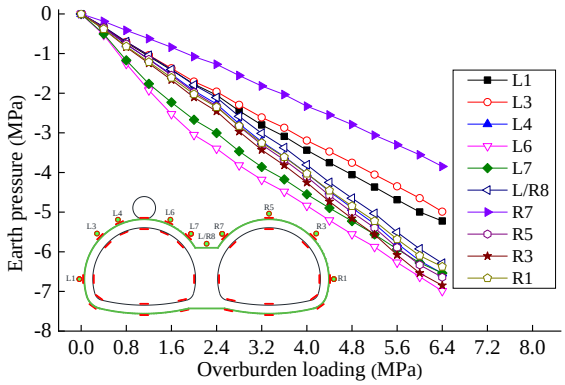

(a) MT1

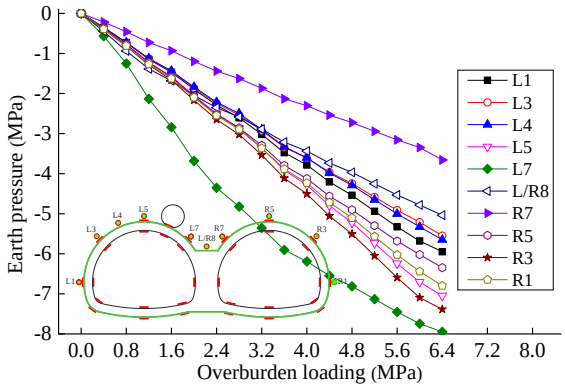

(b) MT2

Fig. 11 Change laws of earth pressure acting on the liner

inside the cavity in MT1 and MT2 was -5 kN·m and -56 kN·m, respectively. The value of -61 kN·m appeared at the liner on the upper right corner of the central wall in MT1.

3.2 Earth pressure distribution

Zhang *et al.* (2019) performed a physical model test, i.e., without cavities behind the liner to investigate the earth pressure distribution of the liner of double-arch tunnels. The maximum value of the earth pressure 0.401 MPa occurred at the vault, and the value of the earth pressure acting on the outside haunch close to sidewalls was slightly larger than that of the inside haunch. The earth pressure acting on the sidewall of the left and right tunnel was 0.359 MPa and 0.368 MPa, respectively (Zhang *et al.* 2019).

Compared with the case with no cavity, the introduction of a cavity obviously changed the distribution of the earth pressure, especially for the region on both sides of cavities. Change laws of the earth pressure acting on the double-arch tunnel liner with overloads are presented in Fig. 11. The distribution of the earth pressure under the same overload of 0.4 MPa (0.01 MPa in the model) is presented in Fig. 12.

The magnitude of the earth pressure vertically acting on the liner of the double-arch tunnels exhibited an increasing trend with the overburden loading. The stress concentration occurred near the boundaries of the cavity. The maximums of the earth pressure appeared on the right side of the cavity, i.e., 0.530 MPa at L6 in MT1 and 0.568 MPa at L7 in MT2. The readings of these two MPs (L6 and L7) increased non-linearly, whereas those of the other MPs generally exhibited

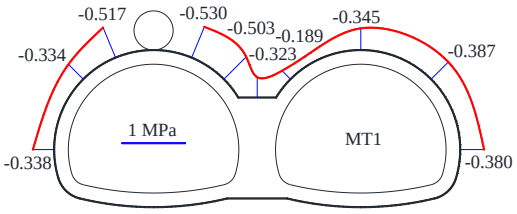

(a) MT1

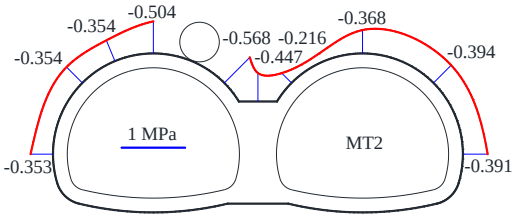

(b) MT2

Fig. 12 Earth pressure distribution (unit: MPa)

a linear relationship. The minimum earth pressure occurred at R7, i.e., 0.189 MPa in MT1 and 0.216 MPa in MT2. With a cavity closer to the central wall, the readings of L/R8, R7, R5, R3, and R1 in MT2 were larger than those in MT1. The cavity in MT2 was closer to the central wall of double-arch tunnels than that in MT1, as a result of larger earth pressure acting on the liner on the opposite side of cavities in MT2. Changes in the location of cavities, significantly impacting the interaction between the soils and the double-arch tunnel liner, resulted in remarkable changes in the earth pressure distribution, especially for the area close to cavities.

Meguid and Kamel (2014) studied the spatial effects of cavities on the earth pressure distribution and the stresses in the pipes. The results revealed the range of changes in the liner stress due to the presence of the cavity behind the liner generally occurred in the areas around the cavity. However, due to the presence of the central wall, the structures of the double-arch tunnels are different from the single tunnels.

3.3 Cracking and liner failure

Distribution of cracks in accordance with the sequence of emergence in the double-arch tunnel liner between MT1 and MT2 is presented in Fig. 13. Herein, the serial numbers indicate the sequential order of cracks in the liner. There are some similarities between MT1 and MT2. The first two cracks successively appeared in the outer fiber of the liner at the bottom of the central wall at a loading level of 0.02 MPa. Two cracks with an opening width of 0.10 mm were noted to propagate in the inner fiber of the invert of a tunnel. Liner cracks also occurred at the arch spring and sidewall, and the mentioned cracks generally have similar appearance and location. The inner fiber of the liners at the arch spring and on the corner of the central wall were all crushing. It seems that the presence of cavities has a slight influence on the lower liner of the double-arch tunnels. However, differences between these two tests are obvious, especially for the liner close to the cavities. Two cracks in the inner fiber of the liner on both sides of the cavity were observed in MT1, while a crack in the outer fiber of the liner inside the cavity was observed in MT2. The crack in

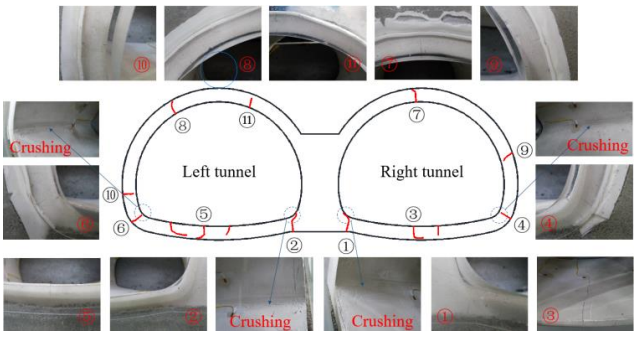

(a) MT1

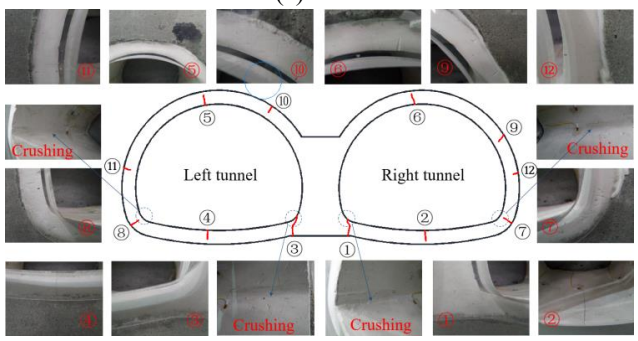

(b) MT2

Fig. 13 Failure pattern of the double-arch tunnel liner

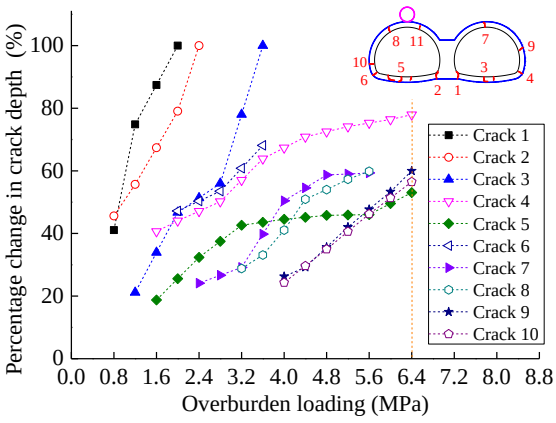

(a) MT1

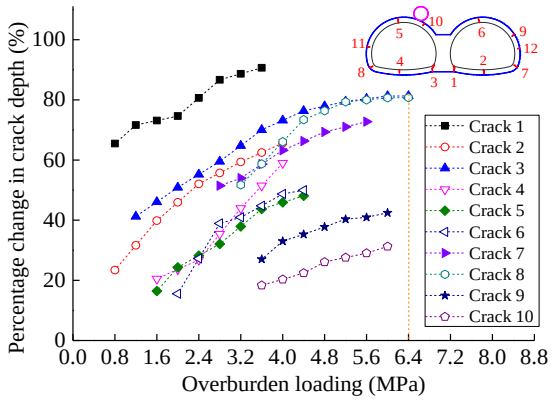

(b) MT2

Fig. 14 Crack depth with respect to the overloading

the inner fiber of the vault on the opposite of the cavity in MT1 appeared later than that in MT2.

The measured crack depth is normalized with respect to

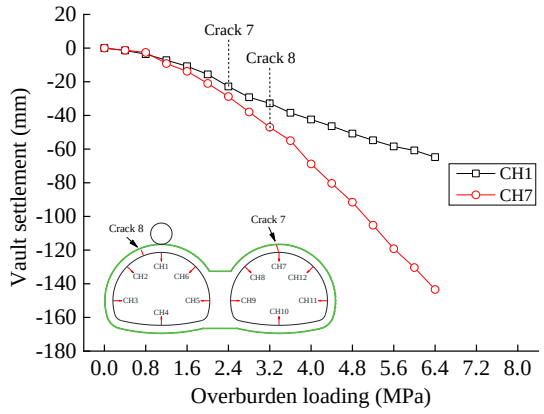

(a) MT1

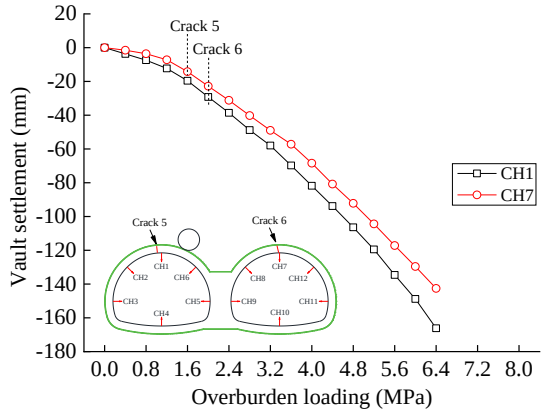

(b) MT2

Fig. 15 Vault settlement development

the liner thick. Given the first ten cracks, the percentage change in crack depth with respect to the overload between MT1 and MT2 are presented in Fig. 14. The crack depth of the liner gradually increased with overloads. The maximum increase in crack depth was found to be about 100% of the thickness of the liner at the bottom of the central wall, which suffered from the most serious failure. It can be seen that the changes in the depth of cracks in the outer fiber of the arch spring ranged from 60% to 80% of the thickness of the liner. The depth of these cracks at the vault and sidewall accounted for approximately 50% of the liner thickness. The results indicate that the depth of cracks at the invert of the double-arch tunnels on the opposite side of the cavity was generally larger than that on the same side of the cavity.

3.4 Tunnel vault settlement

Change laws of the vault settlement with the overburden loading between MT1 and MT2 are presented in Fig. 15. The magnitude of the vault settlement generally exhibited an increasing trend with the overloads. Herein, the serial numbers indicate the sequential order of cracks in the liner near the vault of double-arch tunnels, as shown in Fig. 13. Due to the presence of cavities behind the liner, differences between these two tests are obvious. At a loading level of 6.4 MPa (0.16 MPa in the model), the vault settlement of the left and right tunnel in MT1 is 64.8 mm and 143.4 mm, respectively; the vault settlement of the two tunnels in MT2 is 166.2 mm and 142.6 mm, respectively. The changes in the location of cavity between MT1 and MT2 resulted in small changes in the vault settlement of the right tunnel. It is worth noting that the twin displacement testing devices were installed after the completion of the prepared ground. It indicates that the readings obtained from the displacement meters reveal the liner deformation induced by overloads.

4. Safety analysis of double-arch tunnels

4.1 Evaluation index and method

According to the design specification of the road tunnel (Ministry of Communications of the People's Republic of China 2004), the ultimate load-bearing capacity of the liner subjected to the eccentric compression is calculated in light of the ultimate strength of concrete. By comparing with the actual thrust force, determine the safety factor (K) regarded as the most intuitive index to evaluate the safety of the liner (Xu *et al.* 2019a). The calculation method is as follows:

$$K = \frac{N_0}{N} \geq K_0 \tag{5}$$

where K is the calculated safety factor; N_0 is the ultimate load-bearing capacity of the liner; N is the thrust force; K_0 is the safety factor recommended in the specification, i.e., 2.4 when concretes achieve ultimate compressive strength and 3.6 when concretes achieve ultimate tensile strength.

(1) For $e_0 \leq 0.20\ h$, (e_0 is the eccentricity of thrust force, h is the thick of liner) N_0 is determined by the compressive strength of concrete. Thus, K_1 is calculated using Eq. (6)

$$K_1 = \frac{\varphi \alpha R_a b h}{N} \tag{6}$$

where φ is the longitudinal bending coefficient of liner, R_a is the compressive strength of concrete; b is the width of the liner; α is the eccentric effect factor of thrust force:

$$\alpha = 1 + 0.648(e_0 / h) - 12.569(e_0 / h)^2 + 15.444(e_0 / h)^3 \tag{7}$$

where $e_0 = M / N$, M is bending moment, N is the thrust force.

(2) For $e_0 > 0.20\ h$, N_0 is determined by the tensile strength of concrete. Thus, K_2 is calculated using Eq. (8)

$$K_2 = \frac{1.75 R_t b h \varphi}{N\left(\frac{6e_0}{h} - 1\right)} \tag{8}$$

where R_t is the tensile strength of concrete.

4.2 Results of safety analysis

The distribution of safety factors of the liner at a loading level of 0.4 MPa in the prototype is presented in Fig. 16. Based on N and M in the liner at the bottom of the central wall, K_2 is calculated using Eq. (8). The minimum safety

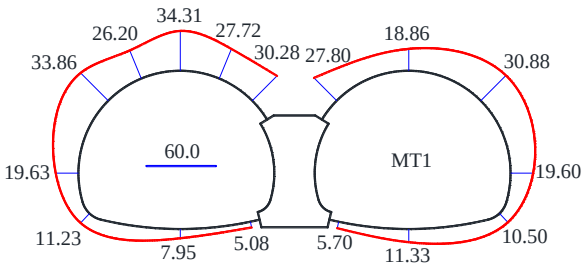

(a) MT1

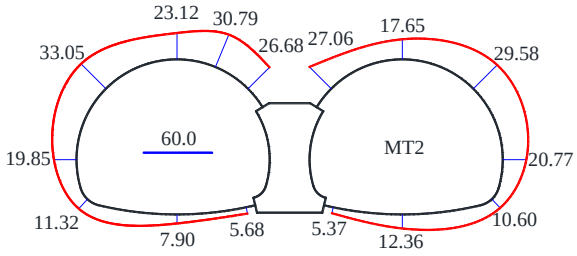

(b) MT2

Fig. 16 Distribution of safety factors of the liner

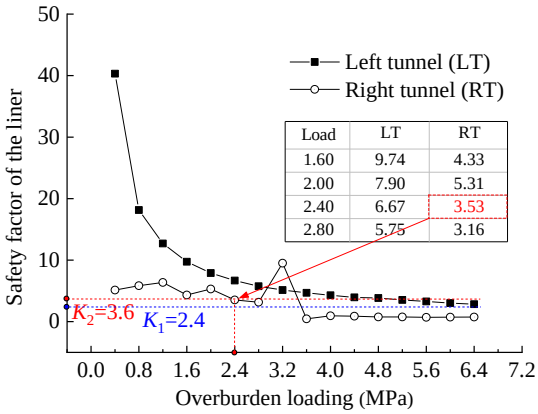

(a) MT1

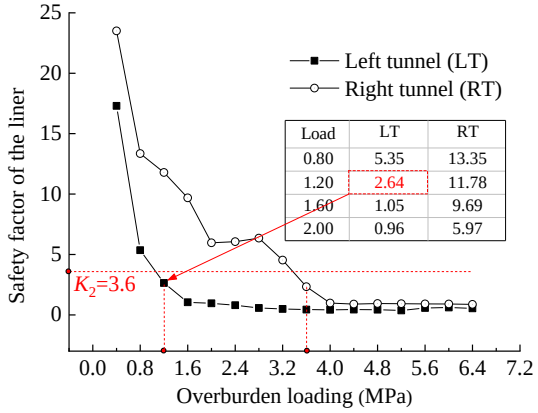

(b) MT2

Fig. 17 Changes in safety factors at the vault

factor in MT1 and MT2 is 5.08 and 5.37, respectively, which are all larger than 3.6. These values indicate that the liner is safe. The safety factor of the liner on the corner of the central wall is smallest. The safety factors of the lower liner, i.e., the central wall, invert and arch spring are smaller than those in other locations of the double-arch tunnels. In this study, the results of the model tests reveal that the first crack is noted to propagate in the outer fiber of the liner on the corner of the central wall of the double-arch tunnels, which is the key zone for safety control. The changes in the safety factors at the vault of the left and right tunnel with the overburden loading are presented in Fig. 17.

It can be seen from Fig. 16 that changes in the location of the cavities behind the liner significantly affect the distribution of the safety factors of the liner close to the cavity. In MT1, the load-bearing capacity of the vault of the left tunnel was controlled by the compressive strength due to $e_0 \leq 0.20$, the value of K_1 of the liner within the cavity is 34.31. In MT2, the load-bearing capacity of the vault of the left tunnel was controlled by the tensile strength due to $e_0 > 0.20$, the value of K_2 of the liner on the left side of the cavity, i.e., the vault of the left tunnel, is 23.12. The value of K_1 of the liner at the right haunch of the left tunnel close to the central wall in MT1 is 30.28, which is larger than 26.68 in MT2. Moreover, the safety factor of the liner at the right shoulder of the left tunnel in MT1 and MT2 is 27.72 and 30.79, respectively. It can be seen from Fig. 17(a) that the minimum value of K_1 is 2.84 in MT1 and more than 2.4, which indicates that the liner at the vault of the left tunnel is safe all the time. For the vault of the right tunnel controlled by the tensile strength, when the overload reached to 2.4 MPa, K_2 was 3.53 in MT1 and less than 3.6. It can be seen from Fig. 17(b) that when the overload reached to 1.2 MPa, K_2 at the vault of the left tunnel was 2.64 in MT2.

4.3 Proposal of preventive measures

As mentioned above, the lower liner at the invert (Area II) became the weak region of the double-arch tunnels, and stress concentration points were created in the outer fiber of the liner at the bottom of the sidewall (Area III) and the central wall (Area I), as shown in Fig. 18.

In order to prevent the failure of the liner at the invert of double-arch tunnels, based on a completed similar double-arch tunnel case in China, it is suggested that grouting pipes with a diameter of 108 mm, 9 m long each (Type I) should be installed at the bottom of the sidewall to reduce the concentrated force in Area III and grouting pipes with a diameter of 45 mm, 4.5 m long each (Type II) should be installed at the bottom of the invert to reinforce the soils below the invert in Area II. Due to the most serious

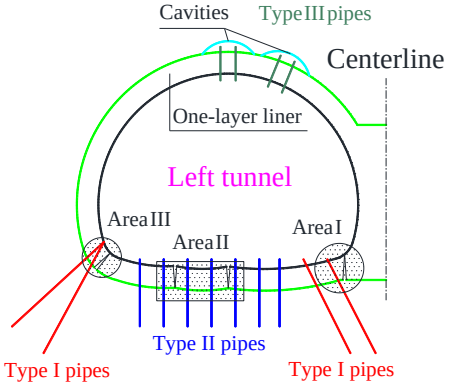

Fig. 18 Sketch of preventive measures

failure of the liner on the corner of the central wall, it is suggested that grouting into and around the double-arch tunnel should be performed to reinforce the ground below the central wall. The Type I pipes are installed in Area I, which is primarily employed to reinforce the foundation soils to enable an effective load transfer. A grout mixture that was composed of ordinary Portland cement, admixture, and sodium silicate was generally selected for the grouting.

In addition, the backfilling injection behind the liner using cement mortar can be adopted to fill cavities that are unintentionally created between the liner and the soils using pre-embedded pipes (Type III), which was beneficial for stabilizing the ground and assuring that the liner maintains contact with the soils (Zhang *et al.* 2018a, Zhang *et al.* 2018b). The control of grouting using both pressure and volume is desired to ensure the safety of the double-arch tunnel construction.

5. Conclusions

Two physical model tests were performed to investigate the impact of cavities behind the liner near the vault on the mechanical and failure behaviors of double-arch tunnels.

- The presence of cavities causes the re-distribution of the earth pressure and induces the stress concentration near the boundaries of cavities, which leads to the bending moments inside the cavity to reverse sign from compression to tension. And it also decreases the thrust forces on both sides of the cavity compared with the case without cavities.
- The liner near the invert becomes the weak region of the double-arch tunnels, and stress concentration points are created in the outer fiber of the liner at the bottom of the sidewall and the central wall. It is suggested that grouting into the foundation soils and backfilling injection behind the liner should be carried out to ensure the tunnel safety.
- Changes in the location of cavities, significantly impact the failure pattern of the liner close to the vault on the same side of the cavity, e.g., cracks appear in the outer fiber of the liner inside the cavity when a cavity is located at the shoulder close to the central wall, which is different from the case that a cavity locates at the vault, whereas changes in the location of cavities have a little influence on the liner at the bottom of the double-arch tunnels.

Acknowledgments

The research was financially supported by the National Natural Science Foundation of China (51868062), Science and Technology Research and Development Program of China Railway Corporation (N2018G029), and Key Laboratory of Urban Underground Engineering of Ministry of Education (TUE2019-02).

References

Chenari, R.J., Fatahi, B., Ghoreishi, M. and Taleb, A. (2019), "Physical and numerical modelling of the inherent variability of shear strength in soil mechanics", *Geomech. Eng.*, **17**(1), 31-45. https://doi.org/10.12989/gae.2019.17.1.031.

Ding, Z.D., Ji, X.F., Li, X.Q., Ren, Z.H. and Zhang, S. (2019), "Influence of symmetric and asymmetric voids on mechanical behaviors of tunnel linings: model tests and numerical simulations", *Symmetry*, **11**(6), 802. https://doi.org/10.3390/sym11060802.

Do, N.A., Oreste, P., Dias, D., Antonello, C., Djeran-Maigre, I. and Livio, L. (2014), "Stress and strain state in the segmental linings during mechanized tunnelling", *Geomech. Eng.*, **7**(1), 75-85. https://doi.org/10.12989/gae.2014.7.1.075.

Fahimifar, A., Ghadami, H. and Ahmadvand, H. (2015), "The ground response curve of underwater tunnels, excavated in a strain-softening rock mass", *Geomech. Eng.*, **8**(3), 323-359. https://doi.org/10.12989/gae.2015.8.3.323.

Fang, Y., Yao, Z.G., Walton, G. and Fu, Y.P. (2018), "Liner behavior of a tunnel constructed below a caved zone", *KSCE J. Civ. Eng.*, **22**(10), 4163-4172. https://doi.org/10.1007/s12205-018-1162-8.

Gao, Y., Jiang, Y.J. and Li, B. (2014), "Estimation of effect of voids on frequency response of mountain tunnel lining based on microtremor method", *Tunn. Undergr. Sp. Technol.*, **42**, 184-194. https://doi.org/10.1016/j.tust.2014.03.004.

Huang, F., Zhu, H.H., Xu, Q.W., Cai, Y.C. and Zhang, X.Y. (2013), "The effect of weak interlayer on the failure pattern of rock mass around tunnel-scaled model tests and numerical analysis", *Tunn. Undergr. Sp. Technol.*, **35**, 207-218. https://doi.org/10.1016/j.tust.2012.06.014.

Huang, H.X., Li, J., Hao, Y.Q. and Dong, X. (2018), "Theoretical explanation of rock splitting based on the micromechanical method", *Geomech. Eng.*, **14**(3), 225-231. https://doi.org/10.12989/gae.2018.14.3.225.

Huang, R.Q. and Xiao, H.B. (2010), "Deformation mechanism of a shallow double-arch tunnel in a sloping rock mass", *Bull. Eng. Geol. Environ.*, **69**(1), 89-97. https://doi.org/10.1007/s10064-009-0240-z.

Jin, L., Wang, T., Jiang, X.A. and Du, X.L. (2019), "Size effect in shear failure of RC beams with stirrups: Simulation and formulation", *Eng. Struct.*, **199**, 109573. https://doi.org/10.1016/j.engstruct.2019.109573.

Jones, S. and Hunt, H. (2011), "Voids at the tunnel-soil interface for calculation of ground vibration from underground railways", *J. Sound Vib.*, **330**(2), 245-270. https://doi.org/10.1016/j.jsv.2010.08.015.

JTG D70-2004 (2004), Code for Design of Road Tunnel, Ministry of Communications of the People's Republic of China, Beijing, China.

Kang, J. M., Song, S., Park, D. and Choi, C. (2017), "Detection of cavities around concrete sewage pipelines using impact-echo method", *Tunn. Undergr. Sp. Technol.*, **65**, 1-11. https://doi.org/10.1016/j.tust.2017.02.002.

Kravitz, B., Mooney, M., Karlovsek, J., Danielson, I. and Hedayat, A. (2019), "Void detection in two-component annulus grout behind a pre-cast segmental tunnel liner using Ground Penetrating Radar", *Tunn. Undergr. Sp. Technol.*, **83**, 381-392. https://doi.org/10.1016/j.tust.2018.09.032.

Lai, J.X., Qiu, J.L., Fan, H.B., Chen, J.X., Hu, Z.N., Zhang, Q. and Wang, J. B. (2017), "Structural safety assessment of existing multiarch tunnel: A case study", *Adv. Mater. Sci. Eng.*, 1697041. https://doi.org/10.1155/2017/1697041.

Lei, M.F., Peng, L.M. and Shi, C.H. (2015), "Model test to investigate the failure mechanisms and lining stress characteristics of shallow buried tunnels under unsymmetrical loading", *Tunn. Undergr. Sp. Technol.*, **46**, 64-75. https://doi.org/10.1016/j.tust.2014.11.003.

Leung, C. and Meguid, M.A. (2011), "An experimental study of

the effect of local contact loss on the earth pressure distribution on existing tunnel linings", *Tunn. Undergr. Sp. Technol.*, **26**(1), 139-145. https://doi.org/10.1016/j.tust.2010.08.003.

Li, S.C., Yuan, C., Feng, X.D. and Li, S.C. (2016), "Mechanical behaviour of a large-span double-arch tunnel", *KSCE J. Civ. Eng.*, **20**(7), 2737-2745. https://doi.org/10.1007/s12205-016-0456-y.

Li, W. and Zhang, C.P. (2020), "Face stability analysis for a shield tunnel in anisotropic sands", *Int. J. Geomech.*, In Press. https://doi.org/10.1061/(ASCE)GM.1943-5622.0001666.

Li, W., Zhang, C.P., Zhu, W.J. and Zhang, D.L. (2019), "Upper-bound solutions for the face stability of a non-circular NATM tunnel in clays with a linearly increasing undrained shear strength with depth", *Comput. Geotech.*, **114**, 103136. https://doi.org/10.1016/j.compgeo.2019.103136.

Li, X.B., Zhang, W., Li, D.Y. and Wang, Q.S. (2008), "Influence of underground water seepage flow on surrounding rock deformation of multi-arch tunnel", *J. Cent. South Univ. Technol.*, **15**(1), 69-74. https://doi.org/10.1007/s11771-008-0015-x.

Li, Y.J., Luo, R., Zhang, Q.H., Xiao, G.X., Zhou, L.M. and Zhang, Y.T. (2017), "Model test and numerical simulation on the bearing mechanism of tunnel-type anchorage", *Geomech. Eng.*, **12**(1), 139-160. https://doi.org/10.12989/gae.2017.12.1.139.

Mansouri, H. and Asghari-Kaljahi, E. (2019), "Two dimensional finite element modeling of Tabriz metro underground station L2-S17 in the marly layers", *Geomech. Eng.*, **19**(4), 315-327. https://doi.org/10.12989/gae.2019.19.4.315.

Meguid, M.A. and Dang, H.K. (2009), "The effect of erosion voids on existing tunnel linings", *Tunn. Undergr. Sp. Technol.*, **24**(3), 278-286. https://doi.org/10.1016/j.tust.2008.09.002.

Meguid, M.A. and Kamel, S. (2014), "A three-dimensional analysis of the effects of erosion voids on rigid pipes", *Tunn. Undergr. Sp. Technol.*, **43**, 276-289. https://doi.org/10.1016/j.tust.2014.05.019.

Meguid, M.A., Saada, O., Nunes, M.A. and Mattar, J. (2008), "Physical modeling of tunnels in soft ground: A review", *Tunn. Undergr. Sp. Technol.*, **23**(2), 185-198. https://doi.org/10.1016/j.tust.2007.02.003.

Min, B., Zhang, X., Zhang, C.P., Gong, Y.P. and Yuan, T.F. (2018), "Mechanical behavior of double-arch tunnels under the effect of voids on the top of the middle wall", *Symmetry*, **10**(12), 703. https://doi.org/10.3390/sym10120703.

Seki, S., Kaise, S., Morisaki, Y., Azetaka, S. and Jiang, Y.J. (2008), "Model experiments for examining heaving phenomenon in tunnels", *Tunn. Undergr. Sp. Technol.*, **23**, 128-138. https://doi.org/10.1016/j.tust.2007.02.007.

Shi, P.X. and Li, P. (2015), "Mechanism of soft ground tunnel defect generation and functional degradation", *Tunn. Undergr. Sp. Technol.*, **50**, 334-344. https://doi.org/10.1016/j.tust.2015.08.002.

Su, J., Jie, Y.M., Niu, X.K., Liu, C. and Liu, X. (2020), "Mechanical behavior of tunnel lining with cracks at different positions", *Symmetry*, **12**(2), 194. https://doi.org/10.3390/sym12020194.

Voznesenskii, A.S. and Nabatov, V.V. (2017), "Identification of filler type in cavities behind tunnel linings during a subway tunnel surveys using the impulse-response method", *Tunn. Undergr. Sp. Technol.*, **70**, 254-261. https://doi.org/10.1016/j.tust.2017.07.010.

Wang, J.F., Huang, H.W., Xie, X.Y. and Bobet, A. (2014), "Void-induced liner deformation and stress redistribution", *Tunn. Undergr. Sp. Technol.*, **40**, 263-276. https://doi.org/10.1016/j.tust.2013.10.008.

Wang, S.M., Jian, Y.Q., Lu, X.X., Ruan, L., Dong, W.J. and Feng, K. (2019), "Study on load distribution characteristics of secondary lining of shield under different construction time", *Tunn. Undergr. Sp. Technol.*, **89**, 25-37. https://doi.org/10.1016/j.tust.2019.03.010.

Wang, S.R., Li, C.L., Li, D.J., Zhang, Y.B. and Hagan, P. (2016), "Skewed pressure characteristics induced by step-by-step excavation of a double-arch tunnel based on infrared thermography", *Thech. Vjesn.*, **23**(3), 827-833. https://doi.org/10.17559/TV-20151217142924.

Xin, C.L., Wang, Z.Z. and Gao, B. (2018), "Shaking table tests on seismic response and damage mode of tunnel linings in diverse tunnel-void interaction states", *Tunn. Undergr. Sp. Technol.*, **77**, 295-304. https://doi.org/10.1016/j.tust.2018.03.010.

Xu, G.W., He, C., Lu, D.Y. and Wang, S.M. (2019a), "The influence of longitudinal crack on mechanical behavior of shield tunnel lining in soft-hard composite strata", *Thin-Wall. Struct.*, **144**, 106282. https://doi.org/10.1016/j.tws.2019.106282.

Xu, G.W., He, C., Yang, Q.H. and Wang, B. (2019b), "Progressive failure process of secondary lining of a tunnel under creep effect of surrounding rock", *Tunn. Undergr. Sp. Technol.*, **90**, 76-98. https://doi.org/10.1016/j.tust.2019.04.024.

Yan, Q.X., Zhang, C., Lin, G. and Wang, B. (2017), "Field monitoring of deformations and internal forces of surrounding rocks and lining structures in the construction of the Gangkou double-arched tunnel–A case study", *Appl. Sci.*, **7**(2), 169. https://doi.org/10.3390/app7020169.

Yang, X.L. and Yan, R.M. (2015), "Collapse mechanism for deep tunnel subjected to seepage force in layered soils", *Geomech. Eng.*, **8**(5), 741-756. https://doi.org/10.12989/gae.2015.8.5.741.

Yasuda, N., Tsukada, K. and Asakura, T. (2017), "Elastic solutions for circular tunnel with void behind lining", *Tunn. Undergr. Sp. Technol.*, **70**, 247-285. https://doi.org/10.1016/j.tust.2017.08.032.

Yasuda, N., Tsukada, K. and Asakura, T. (2019), "Three-dimensional seismic response of a cylindrical tunnel with voids behind the lining", *Tunn. Undergr. Sp. Technol.*, **84**, 399-412. https://doi.org/10.1016/j.tust.2018.11.026.

Ye, Z.J., Zhang, C.P., Ye, Y. and Zhu, W.J. (2020), "Application of transient electromagnetic radar in quality evaluation of tunnel composite lining", *Constr. Build. Mater.*, **240**, 117958. https://doi.org/10.1016/j.conbuildmat.2019.117958.

Zhang, C.P., Han, K.H. and Zhang, D.L. (2015), "Face stability analysis of shallow circular tunnels in cohesive-frictional soils", *Tunn. Undergr. Sp. Technol.*, **50**, 345-357. https://doi.org/10.1016/j.tust.2015.08.007.

Zhang, C.P., Li, W., Zhu, W.J. and Tan, Z.B. (2020), "Face stability analysis of a shallow horseshoe-shaped shield tunnel in clay with a linearly increasing shear strength with depth", *Tunn. Undergr. Sp. Technol.*, **97**, 103291. https://doi.org/10.1016/j.tust.2020.103291.

Zhang, C.P., Zhang, X. and Fang, Q. (2018a), "Behaviors of existing twin subway tunnels due to new subway station excavation below in close vicinity", *Tunn. Undergr. Sp. Technol.*, **81**, 121-128. https://doi.org/10.1016/j.tust.2018.07.020.

Zhang, X., Ye, Z.J., Min, B. and Xu, Y.J. (2019), "Effect of voids behind lining on the failure behavior of symmetrical double-arch tunnels", *Symmetry*, **11**(10), 1321. https://doi.org/10.3390/sym11101321.

Zhang, X., Zhang, C.P. and Wang, J.C. (2018b), "Effect of closely spaced twin tunnel construction beneath an existing subway station: A case study", *J. Test. Eval.*, **46**(4), 1159-1573. https://doi.org/10.1520/JTE20160563.

Zhang, Y.X., Shi, Y.F., Zhao, Y.D., Fu, L.R. and Yang, J.S. (2017), "Determining the cause of damages in a multiarch tunnel structure through field investigation and numerical analysis", *J. Perform. Constr. Fac.*, **31**(3), 04016104. https://doi.org/10.1061/(ASCE)CF.1943-5509.0000981.

Zhao, Y.D., Liu, C., Zhang, Y.X., Yang, J.S. and Feng, T.G. (2019),

"Damaging behavior investigation of an operational tunnel structure induced by cavities around surrounding rocks", *Eng*. *Fail*. *Anal*., **99**, 203-209. https://doi.org/10.1016/j.engfailanal.2019.02.023.

CC